

Article

Sn(IV)porphyrin-Anchored TiO₂ Nanoparticles via Axial-Ligand Coordination for Enhancement of Visible Light-Activated Photocatalytic Degradation

Nirmal Kumar Shee and Hee-Joon Kim * Department of Chemistry and Bioscience, Kumoh National Institute of Technology,
Gumi 39177, Republic of Korea; nirmalshee@gmail.com

* Correspondence: hjk@kumoh.ac.kr; Tel.: +82-54-4787822

Abstract: A visible-light-active photocatalyst, SnP/AA@TiO₂, was fabricated by utilizing the coordination chemistry between the axial hydroxo-ligand in the (*trans*-dihydroxo)(5,10,15,20-tetraphenylporphyrinato)Sn(IV) complex (SnP) and adipic acid (AA) on the surface of TiO₂ nanoparticles. The SnP center was strongly bonded to the surface of the TiO₂ nanoparticles via the adipic acid linkage in SnP/AA@TiO₂, as confirmed by various instrumental techniques. SnP/AA@TiO₂ exhibited remarkably enhanced photocatalytic activity toward the degradation of rhodamine B dye (RhB) in aqueous solution under visible-light irradiation. The RhB degradation efficiency of SnP/AA@TiO₂ was 95% within 80 min, with a rate constant of 0.0366 min⁻¹. The high degradation efficiency, low catalyst loading and high reusability make SnP-anchored photocatalysts more efficient than other photocatalysts, such as TiO₂ and SnP@TiO₂.

Keywords: Sn(IV)porphyrin; TiO₂; adipic acid; photocatalyst; degradation of dye



Citation: Shee, N.K.; Kim, H.-J. Sn(IV)porphyrin-Anchored TiO₂ Nanoparticles via Axial-Ligand Coordination for Enhancement of Visible Light-Activated Photocatalytic Degradation. *Inorganics* **2023**, *11*, 336. <https://doi.org/10.3390/inorganics11080336>

Academic Editors: Alejandro Pérez-Larios and Oomman K. Varghese

Received: 19 July 2023

Revised: 31 July 2023

Accepted: 9 August 2023

Published: 15 August 2023



Copyright: © 2023 by the authors. Licensee MDPI, Basel, Switzerland. This article is an open access article distributed under the terms and conditions of the Creative Commons Attribution (CC BY) license (<https://creativecommons.org/licenses/by/4.0/>).

1. Introduction

With the increasing development of civilization and industrialization, environmental pollution has become a serious problem affecting ecosystems, biodiversity and human health worldwide. Every year, the leather, textile, drugs and paper printing industries discharge large amounts of toxic compounds, such as organic dyes, pesticides, herbicides, pigments, plasticizers, biphenyls, phenols, nitro and amino compounds, into water bodies. These organic chemicals not only deteriorate the potability of these water sources but also have negative effects on aquatic life (flora and fauna) [1,2]. This has led to increasing scientific efforts to develop strategies for environmental remediation by wastewater treatment in the environmental and research fields [3,4]. Currently, various physicochemical methods, including adsorption [5], filtration [6], chemical coagulation [7], precipitation [8], bacterial treatment [9], electrochemical methods [10] and advanced oxidation processes (AOPs) [11], are utilized for the removal of these hazardous compounds from wastewater. Undoubtedly, AOPs are the most promising techniques for the remediation of wastewater due to their simple operation, low cost and high efficiency in degrading hazardous pollutants to less-toxic CO₂ and H₂O without the generation of secondary pollution. In AOP methods, visible light is absorbed by a photocatalyst, which subsequently generates reactive oxygen species (ROS) in situ, thereby accelerating the degradation of pollutant chemicals. Light absorption and ensuing electron transfer are the key factors for obtaining photocatalysts with efficient solar energy conversion [12,13].

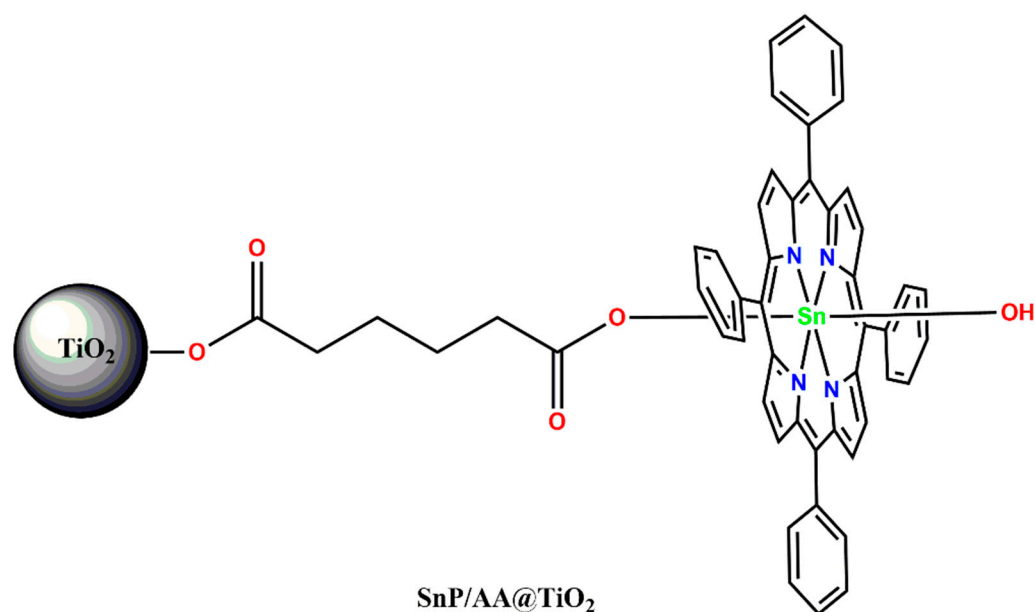
In general, nanoscale materials display distinctive optical and electronic properties, depending on the size and shape of the photo-functional materials. Considering the advantages of photocatalytic processes, various organic and inorganic-based nanomaterials, such as ZnO [14], TiO₂ [15], graphitic carbon nitride (g-C₃N₄) [16], zeolites [17], metal-organic framework (MOF) [18], bismuth-based photocatalysts [19], carbon quantum dots

(CQDs) [20], fullerene [21], graphene oxide or reduced graphene oxide (GO and RGO) [22] and porphyrin-based nanostructures [23], have been used to remove toxic compounds from wastewater. Among them, TiO_2 and related materials have earned distinction as promising photocatalysts due to their high stability, low toxicity, low cost and high catalytic efficiency in degrading hazardous chemicals in water. The large bandgap (~ 3.2 eV) of these catalysts restricts the absorption of the solar spectrum in the visible region and results in low photocatalytic efficiency. A large amount of catalyst is required to achieve effective degradation rates in the photocatalytic process [24].

On the other hand, because of their high absorption coefficient in the regions of 400–440 nm (Soret band) and 500–720 nm (Q bands), porphyrinoids (free-base porphyrins or metalloporphyrins) are capable of absorbing light over a wider range (UV and visible), which facilitates the generation of ROS through a spin-forbidden intersystem crossing mechanism [25,26]. The inherent aromatic electronic features and rigid structural skeleton of porphyrinoids facilitate their self-aggregation in solution [27,28]. The use of porphyrinoid compounds in photocatalysis is limited by the proneness of these compounds to fast deactivation, easy agglomeration in solution and poor reusability. The development of new photocatalysts that overcome all of the above-mentioned drawbacks remains a challenge. For this purpose, porphyrinoid compounds have been immobilized on solid supports, such as matrices [29], hydrogels [30], zeolites [31] and nano- or microparticles [32–35], where the resulting hybrid materials show outstanding photocatalytic activity compared to that of the starting porphyrinoid compounds. After entrapping porphyrinoid compounds on solid supports, the resultant hybrid materials exhibit increased solar absorption/harvesting capabilities, as well as enhanced electronic conductivity mediated by intimate chemical contacts. The rigid framework of these hybrids is resistant to hydrolysis and increases the chemical and physical stability for further use.

Previously, we and others immobilized Sn(IV)porphyrins on TiO_2 to construct nano-hybrid materials for photocatalysis [36–38]. Sn(IV)porphyrin complexes were selected because they are outstanding building blocks for constructing functional porphyrin nanomaterials for the photocatalytic degradation of organic pollutant dyes [39–44]. Sn(IV)porphyrin centers are oxophilic and can form stable 6-coordinate complexes with two *trans*-axial oxyanion ligands (alkoxides and carboxylates) [45–54]. In this study, the axial coordination chemistry of Sn(IV)porphyrins is utilized to construct SnP/AA@ TiO_2 as a hybrid nanomaterial for water remediation. Sn(IV)porphyrin complexes, as visible-light sensitizers, are anchored on the surface of TiO_2 nanoparticles by bridging via adipic acid, as depicted in Scheme 1. SnP@ TiO_2 was also prepared by directly anchoring Sn(IV)porphyrin complexes without the bridging adipic acid molecules.

To evaluate the photocatalytic activity for the degradation of organic dyes under visible-light irradiation, we consider rhodamine B (RhB) dye as a model pollutant in this study. RhB is a water-soluble, organic amino xanthene dye. It is widely used as a coloring agent in the printing, textile, leather and cosmetic industries. It is one of the 20 dyes detected most frequently in wastewater, and it irritates the skin and eyes and damages the respiratory, reproductive and nervous systems. Even at low concentrations, RhB dye is carcinogenic. RhB dye is very stable in aqueous solutions and non-biodegradable. It is imperative to find an effective oxidation system for removing this pollutant dye from wastewater [55–65]. We investigate the photocatalytic degradation of RhB using Sn(IV)porphyrin-anchored TiO_2 photocatalysts. The degradation efficiency of SnP/AA@ TiO_2 is compared with that of SnP@ TiO_2 , and the kinetics and the mechanism of the degradation process are also discussed.



Scheme 1. Chemical structure of SnP/AA@TiO₂.

2. Results and Discussion

2.1. Fabrication and Characterization of Photocatalysts

The synthesis of SnP/AA@TiO₂ has been described in the experimental section, where the surface of the TiO₂ nanoparticles was firstly functionalized with adipic acid, after which SnP was anchored by forming a chemical Sn–O₂C bond through the interaction of the axial OH ligand of the Sn(IV)porphyrin and COOH group of adipic acid to afford the SnP/AA@TiO₂ composite. The above reaction was also performed without treating the nanoparticles with adipic acid, affording the SnP@TiO₂ composite. The surface modifications for generating SnP/AA@TiO₂ and SnP@TiO₂ were confirmed by analyzing the zeta potential, which is calculated by the degree of electrostatic repulsion of the composite surface. The average zeta potentials of pure TiO₂ and the SnP@TiO₂ and SnP/AA@TiO₂ composites were measured in aqueous solutions at pH 7, with respective values of −6.97, −4.87 and 7.02 mV. The more negative value for pure TiO₂ is mainly due to the presence of electronegative oxygen atoms on the surface. In contrast, the high positive zeta potential of SnP/AA@TiO₂ compared to that of pure TiO₂ and SnP@TiO₂ indicates that Sn(IV)porphyrins sufficiently covered the surface of TiO₂ over a large area in the former. As expected, this immobilization was successfully achieved through chemical anchoring via the adipic acid linkage. On the other hand, the zeta potential of SnP@TiO₂ was less negative than that of pure TiO₂. The presence of hydroxyl groups on the surface of TiO₂ is essential for the formation of Sn–O–Ti bonds in SnP@TiO₂. This is because hydroxo-Sn(IV)porphyrin complexes undergo dehydrating condensation with OH or COOH groups to yield covalently bonded moieties, such as Sn–O–Ti. However, the main linkages on the surface of TiO₂ are O–Ti–O groups, which remain intact or may physically adsorb SnP species via weak hydrogen bonding to form species such as Ti–O···HO–SnP. The amount of adsorbed porphyrin (SnP) was estimated from the Sn content of the hybrid composites (SnP/AA@TiO₂ or SnP@TiO₂) by ICP analysis. The determined amount of SnP in SnP/AA@TiO₂ and SnP@TiO₂ was 0.149 and 0.042 mmol/g, respectively.

The FT-IR spectra of SnP, TiO₂, SnP@TiO₂ and SnP/AA@TiO₂ are depicted in Figure 1. The FT-IR spectrum of SnP shows vibrational peaks at 790 and 1024 cm^{−1}, attributed to the out-of-plane bending vibration of C–H and the in plane bending vibration of C–H in the benzene ring, respectively. The peaks at 1406, 1591 and 3384 cm^{−1} are designated to the stretching vibrations of C–N, C=C and C–H in the pyrrole ring, respectively. The peak at 3601 cm^{−1} is assigned to the stretching vibration of the OH of the axial hydroxyl group in the Sn(IV) porphyrin. The strong peaks at 855–515 cm^{−1} are characteristic peaks

of Ti–O–Ti stretching in TiO₂. The FT-IR spectrum of SnP@TiO₂ showed the characteristic band of Ti–O–Ti stretching at 595 cm⁻¹. A very broad band was also observed at 3450 cm⁻¹, corresponding hydrogen-bonded OH groups. All other peaks remained unchanged or were slightly modified relative to those of the starting components. For SnP/AA@TiO₂, the characteristic carboxylate stretching band of AA shifted from 1685 to 1690 cm⁻¹ upon complexation with SnP. All other peaks remained unchanged or were slightly changed relative to those of SnP@TiO₂. These observations indicate that the characteristic linkages of SnP and TiO₂ remained intact in the composites (SnP/AA@TiO₂ or SnP@TiO₂).

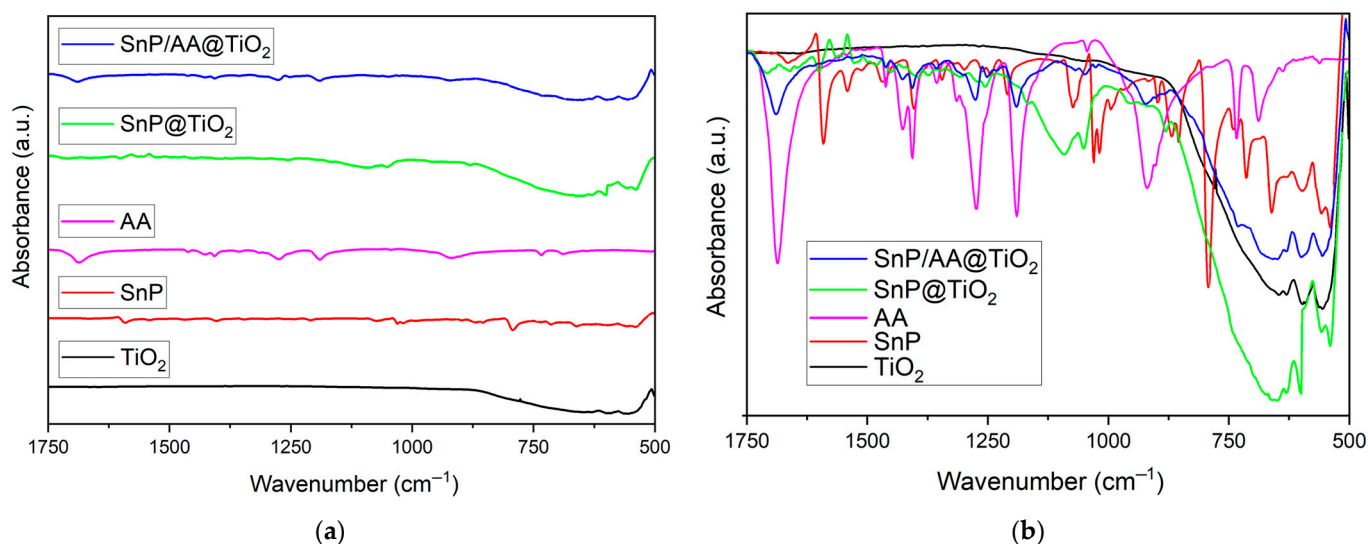


Figure 1. FT-IR spectra of (a) SnP, TiO₂, SnP@TiO₂ and SnP/AA@TiO₂; (b) magnified views in the range of 1750–500 cm⁻¹.

Solid-state UV-vis spectroscopy was used to evaluate the light absorption properties of SnP, TiO₂, SnP@TiO₂ and SnP/AA@TiO₂ (Figure 2). The spectrum of SnP shows a strong absorption band at 427 nm, assigned as the Soret band, and two weak absorption bands at 566 and 606 nm corresponding to the Q bands. The spectrum of pure TiO₂ showed only one strong absorbance band at 359 nm in the UV region. In the visible light region, a strong and very broad absorption band was centered at 440 nm in the spectrum of SnP/AA@TiO₂, which is the Soret band, along with four weak bands at 523, 565, 603 and 626 nm, which are the Q bands. The absorption pattern of SnP@TiO₂ was similar. Accordingly, SnP/AA@TiO₂ and SnP@TiO₂ are expected to have enhanced light-harvesting ability in most of the visible light regions. The bandgap energy (E_g) calculated from the Tauc plot was ~2.42 eV for SnP/AA@TiO₂, which is narrower than that of SnP (~2.96 eV), TiO₂ (~3.12 eV) and SnP@TiO₂ (~2.75 eV). The enhanced light absorption and narrower bandgap of SnP/AA@TiO₂ can effectively improve solar energy utilization to generate more photogenerated reactive species that can participate in the photocatalytic degradation of organic pollutants.

The fluorescence spectra are presented in Figure 3. The spectrum of SnP showed a single fluorescence peak at 654 nm, and that of the SnP/AA@TiO₂ composite exhibited two fluorescence peaks at 630 and 650 nm. On the other hand, the spectrum of SnP@TiO₂ showed a broad fluorescence peak that seems to be a combination of the peaks of SnP and SnP/AA@TiO₂. Note that under excitation at 550 nm, pure TiO₂ showed no fluorescence signal. A comparison of the spectral features suggests that the immobilization mode of the SnP molecules in SnP/AA@TiO₂ and SnP@TiO₂ is different, which is consistent with the zeta potential analysis discussed above.

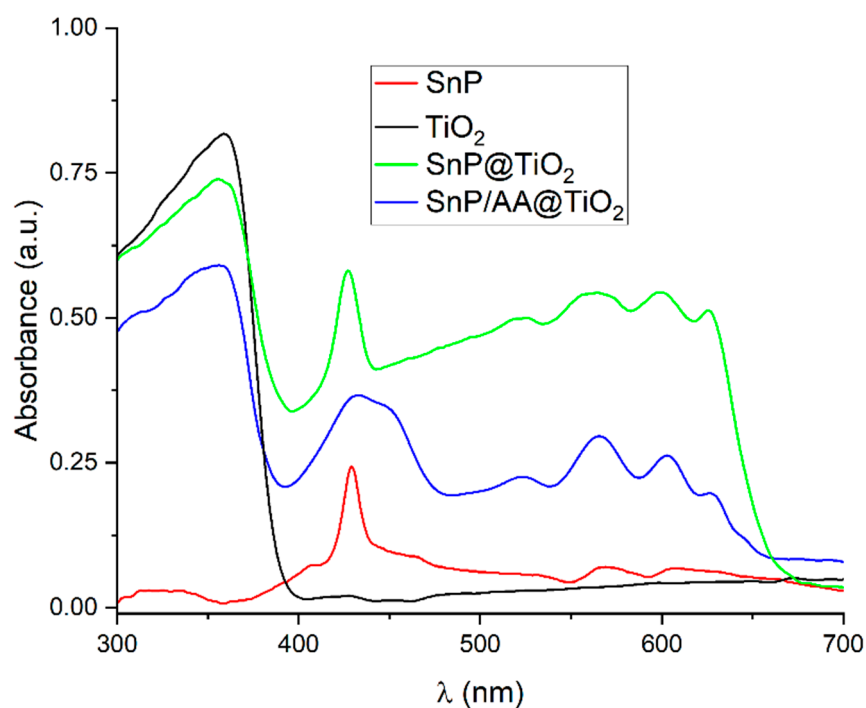


Figure 2. Solid state UV-vis absorption spectra of SnP, TiO₂, SnP@TiO₂ and SnP/AA@TiO₂ in Nujol.

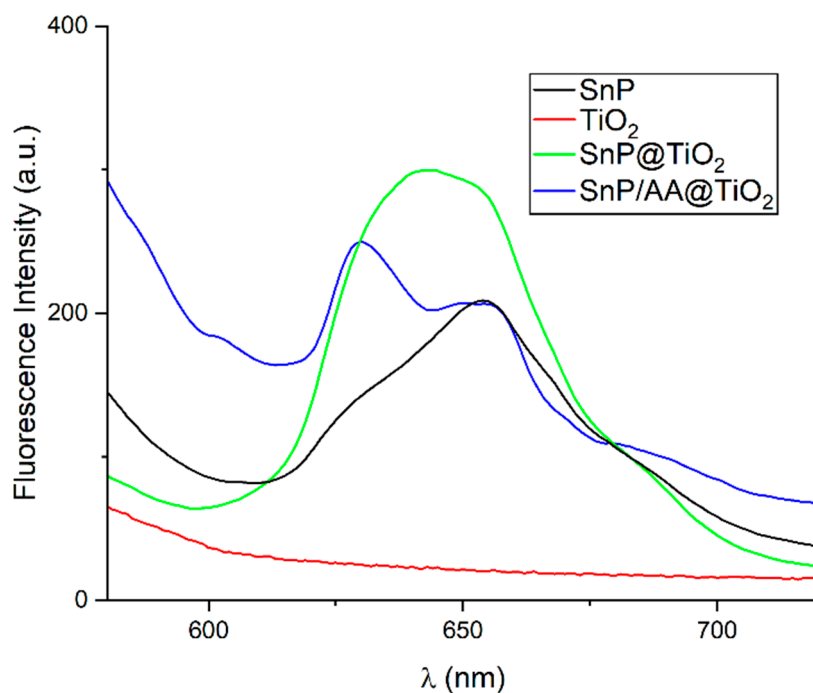


Figure 3. Fluorescence spectra of SnP, TiO₂, SnP@TiO₂ and SnP/AA@TiO₂ in Nujol ($\lambda_{\text{ex}} = 550 \text{ nm}$).

The morphological developments of the synthesized composites were examined by field-emission scanning electron microscopy (FE-SEM). The morphologies of SnP@TiO₂ and SnP/AA@TiO₂, along with those of the starting compounds, are presented in Figure 4. SnP did not develop any well-defined nano-scale morphology (Figure 4a), whereas TiO₂ comprised regularly shaped particles with an average diameter in the range of 145–305 nm (Figure 4b). Compared to TiO₂, the shape and size remained almost unchanged for SnP@TiO₂ (Figure 4c). In contrast, SnP/AA@TiO₂ had a flower-like, fused morphology, which is different from that of SnP, TiO₂ and SnP@TiO₂. The elemental distribution in the

composite (SnP/AA@TiO₂) was investigated using energy-dispersive X-ray (EDX) mapping (Figure S1). Ti, O, Sn, N and C were evenly distributed in the composite, indicating that SnP was well immobilized on the TiO₂ nanoparticles.

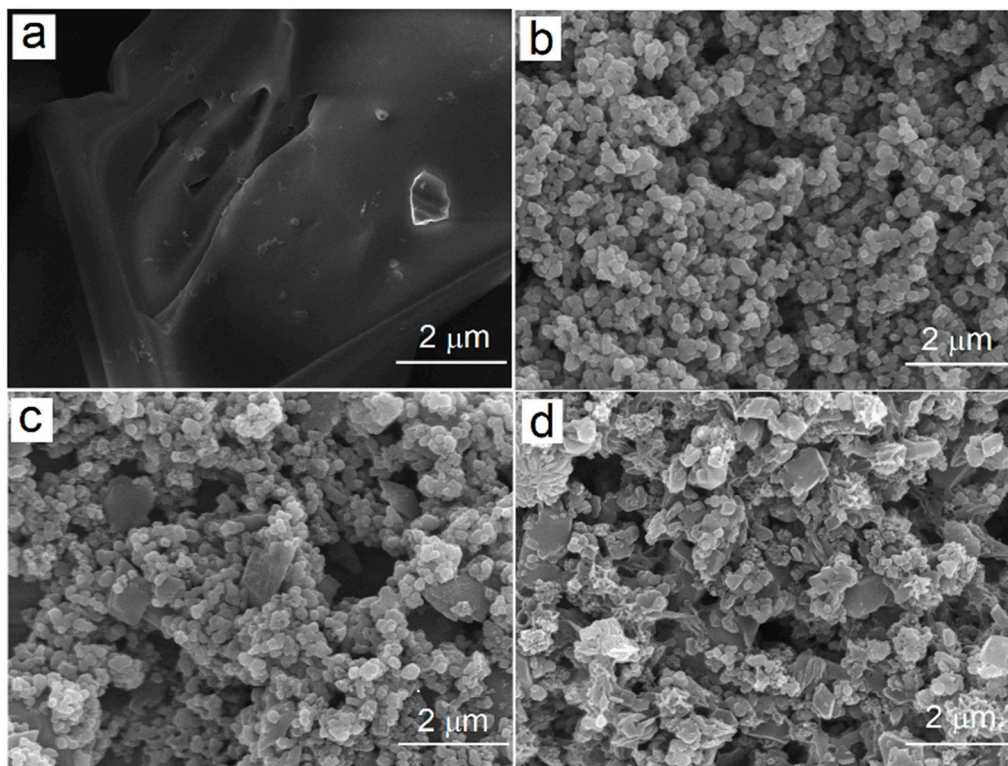


Figure 4. FE-SEM images of SnP (a), TiO₂ (b), SnP@TiO₂ (c) and SnP/AA@TiO₂ (d).

The TGA curves of the samples are displayed in Figure S2. TiO₂ exhibited only a slight weight loss (~1 wt%) between 50 °C and 600 °C, compared to 2.12 wt% for SnP@TiO₂ and 3.26 wt% for SnP/AA@TiO₂ in the range of 200–440 °C. The high thermal decomposition temperatures of the composites suggest a successful combination of the molecular components. SnP@TiO₂ and SnP/AA@TiO₂ possess moderate specific surface areas of 62.21 and 77.37 m²g⁻¹, respectively (Figure S3). The composites also exhibit type-IV adsorption-desorption isotherms, demonstrating the mesoporous nature of the surface of the composites. The data indicate that SnP molecules were successfully anchored on the surface of the TiO₂ nanoparticles to form SnP/AA@TiO₂ and SnP@TiO₂ composite structures with high thermal stability and a large surface area. The characteristics of these composite nanoparticles, revealed by the spectroscopic, SEM, TGA and surface area analyses, indicate their attractive potential as visible-light-activated photocatalysts.

2.2. Photocatalytic Degradation of Rhodamine B (RhB)

The photocatalytic efficiency of SnP/AA@TiO₂ and SnP@TiO₂ was investigated in the degradation of an organic dye under visible-light irradiation in an aqueous medium. We selected rhodamine B (RhB) as the target pollutant dye for the photocatalytic degradation reaction. As shown in Figure S4, a period of ~25 min was required to reach the adsorption-desorption equilibrium, where 3, 14, 18 and 21% of RhB were respectively adsorbed by SnP, TiO₂, SnP@TiO₂ and SnP/AA@TiO₂. The degradation experiment indicates that the high surface area and porous nature of SnP/AA@TiO₂ and SnP@TiO₂ can enhance the adsorption of pollutants and can also promote mass diffusion. Time-dependent absorption spectra of the aqueous solution of RhB dye in the presence of SnP/AA@TiO₂ under visible-light irradiation are shown in Figure S5. Negligible decay of RhB dye was observed in the absence of either visible light or the SnP/AA@TiO₂ photocatalyst (Figure 5). Therefore,

visible light as well as a photocatalyst are required for the degradation of RhB dye. The absorbance of RhB dye at 554 nm decreased as the irradiation time increased (Figure S5). As depicted in Figure 5, all precursors and as-prepared composite catalysts clearly showed significant effectiveness for the photo-degradation of RhB in aqueous solution.

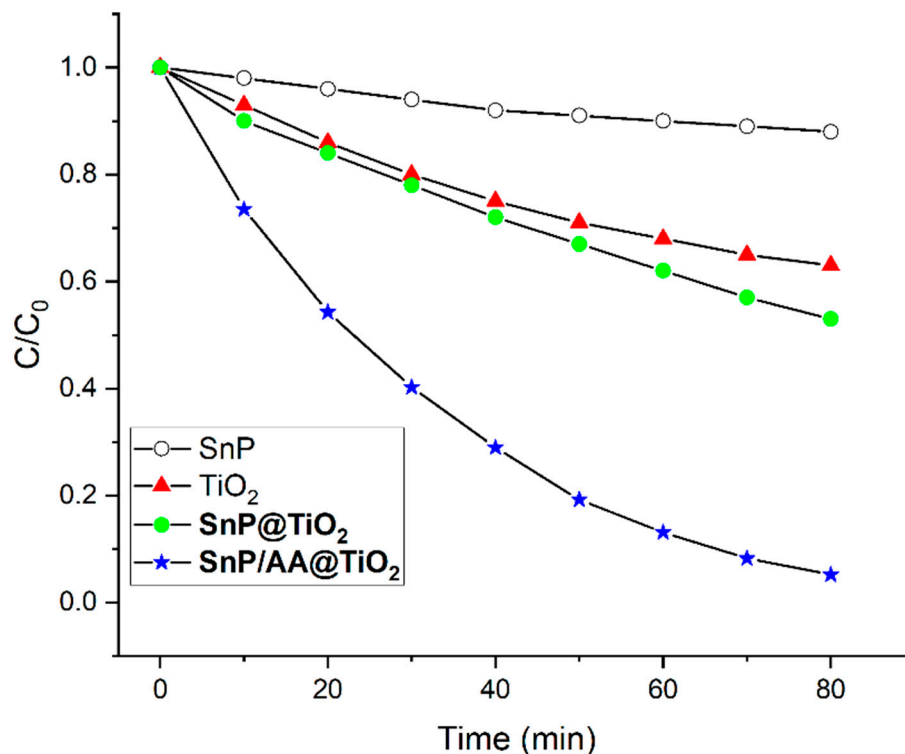


Figure 5. Photocatalytic degradation of the aqueous solution of RhB dye under visible-light irradiation in the presence of SnP/AA@TiO₂, SnP@TiO₂, SnP and TiO₂ ($T = 298$ K, $\text{pH} = 7$).

The degradation of RhB dye in the presence of a photocatalyst can be described by the degradation efficiency, $(C_0 - C)/C_0$, where C_0 is the starting concentration of RhB dye and C is the concentration at time t . The respective degradation rates of RhB in the presence of SnP, TiO₂, SnP@TiO₂ and SnP/AA@TiO₂ were 12, 37, 47 and 95% after 80 min of irradiation of visible light (Figure 5). The SnP/AA@TiO₂ photocatalyst shows superior performance for RhB dye degradation compared to SnP, TiO₂ and SnP@TiO₂. To further elucidate the reaction kinetics for the degradation of RhB dye, we applied the pseudo-first-order theory exhibited by the equation $\ln(C_0/C) = kt$, which is generally used in photocatalytic degradation experiments if the initial concentration of dye (C_0) is low; k is the pseudo-first-order rate constant for degradation experiments. Based on the data plotted in Figure 5, Figure S6 presents the reaction kinetics of RhB dye degradation. The first-order degradation rate constant of RhB dye in the presence of SnP, TiO₂, SnP@TiO₂ and SnP/AA@TiO₂ was calculated as 0.0016, 0.006, 0.0078 and 0.0366 min^{-1} , respectively (Figure S6). The above results are encouraging compared with other reported rate constants for the degradation of RhB dye (Table 1).

Among the developed photocatalysts, SnP/AA@TiO₂ possesses the highest photodegradation rate and can remove ~95% of RhB dye within 80 min. To confirm the effect of TiO₂-immobilized SnP on the photocatalytic activity of the SnP/AA@TiO₂ composite, the weight percentage of SnP in the composite was serially varied and the effect on the degradation of RhB dye was evaluated (Figure S7). The photodegradation of RhB by SnP/AA@TiO₂ containing 30 wt% SnP proceeded much more efficiently than that in the presence of pure SnP or pure TiO₂. When the mass ratio of SnP to TiO₂ in the composite was increased, the dye degradation rate increased and reached a maximum of 30%. The degradation rate increased slightly to 40% or 50%. When the wt% of SnP in SnP/AA@TiO₂

is higher than 30%, SnP molecules agglomerate easily on the surface of TiO₂ to some extent. This reduced the number of reactive sites, restrained the photogenerated charge separation and slowly lowered the degradation rate. This trend suggests that the synergistic effects between SnP and TiO₂ are responsible for the enhanced photocatalytic efficiency of the SnP/AA@TiO₂ composite.

Table 1. Comparison of the photodegradation efficiency of RhB with that of various photocatalysts.

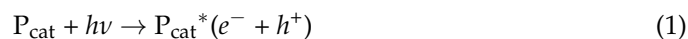
Photocatalyst	Rate Constant (min ⁻¹)	Reference
ZnP-SnP-ZnP triad nanostructure	0.0100	[41]
H ₂ Ti ₃ O ₇ nanotube	0.0020	[55]
TiO ₂ (P-25)	0.0010	[55]
Co _{0.6} Zn _{0.4} Fe ₂ O ₄	0.0150	[56]
TiO ₂	0.0015	[57]
TiO ₂ /MgZnAl	0.0050	[57]
ZnO	0.0090	[58]
ZnO/Burkeite	0.0280	[58]
Ni _{0.5} Zn _{0.5} Al ₂ O ₄	0.0050	[59]
g-C ₃ N ₄	0.0032	[60]
O-g-C ₃ N ₄	0.0790	[60]
SnO ₂ -Acalypha Indica	0.0062	[61]
H ₂ O ₂ @Cu/Al ₂ O ₃ /g-C ₃ N ₄	0.0820	[62]
Au/ZnO	0.0300	[63]
TiO ₂ -SnO ₂ -Al ₂ O ₃	0.0610	[64]
ZnS-NaBH ₄	0.0123	[65]
SnP	0.0016	this study
TiO ₂	0.0060	this study
SnP@TiO ₂	0.0078	this study
SnP/AA@TiO ₂	0.0366	this study

Because the reusability of photocatalysts is very important for practical application, we evaluated the recyclability of SnP/AA@TiO₂ in RhB dye degradation (Figure S8). Even after ten consecutive cycles, SnP/AA@TiO₂ still maintained a high degradation efficiency, with only a 3% reduction, indicating that the SnP/AA@TiO₂ photocatalyst possesses remarkable stability. The stability of this photocatalyst was further confirmed by examining the structure of SnP/AA@TiO₂ after the degradation reaction. The XRD (Figure S9) and FE-SEM (Figure S10) data for used SnP/AA@TiO₂ were almost the same as that of the pristine state, indicating that the properties of this photocatalyst remained intact during the photocatalytic reaction. Moreover, SnP/AA@TiO₂ was easily recovered from the reaction mixture through a successive filter-wash-dry procedure.

To optimize the reaction conditions (RhB dye/photocatalyst ratio, temperature and solution pH), the photodegradation of RhB was performed under several different conditions. Degradation experiments were performed at various temperatures to analyze the effect of temperature on the decay of RhB dye by SnP/AA@TiO₂. Over the temperature range of 290–330 K, the degradation occurred consistently without a significant decrease (Figure S11). Initially, the RhB dye solution was prepared with distilled water at pH 7. The pH of the aqueous RhB dye solution had a notable effect on the degradation rate of RhB dye. It is evident from Figure S12 that the rate of degradation increased when the pH was raised from pH 2 to 7 but decreased when the pH was further increased to 12. Basic pH had a greater effect on the degradation compared to acidic pH. Additionally, the effect of the RhB dye/catalyst ratio on the degradation of RhB dye was examined using various concentrations of RhB solution (10 to 80 mg L⁻¹) with a constant amount of photocatalyst SnP/AA@TiO₂ (50 mg was used in every experiment). Most of the RhB dye was degraded at concentrations of 10–30 mg L⁻¹, and approximately 70% of the dye was degraded even at 80 mg L⁻¹ (Figure S13).

The mechanism of photocatalytic degradation of dye by SnP@TiO₂ is somewhat different from that of SnP/AA@TiO₂. In the case of SnP@TiO₂, when visible light is

absorbed, excited electrons can easily move to the conduction band of TiO₂. These reactive electrons in the conduction band can react with oxygen to produce superoxide radical anions (O₂^{-•}) and degrade RhB dye. TiO₂ holes can react with water to generate hydroxyl radicals (•OH) and degrade RhB dye. On the other hand, when the surface of TiO₂ is modified with SnP via AA, SnP/AA@TiO₂ can behave as a single molecule with lower band gap energy [66,67]. Therefore, the degradation mechanism of SnP/AA@TiO₂ is very similar to other porphyrin-based materials [42–45]. In step 1, the Sn(IV)porphyrin-based photocatalyst (P_{cat}) in an aqueous solution of RhB dye is activated by absorbing visible light. After crossing the bandgap, the valence band (VB) electrons are promoted to the conduction band (CB). This leads to the creation of electron-hole pairs (e⁻/h⁺) pairs on the surface of the photocatalyst. These photo-generated holes (h⁺) subsequently react with H₂O to produce highly reactive hydroxyl radicals (•OH) (step 2). The excited electron reacts with O₂ (dissolves in water) to produce highly reactive superoxide radical anions (O₂^{-•}) in step 3. The above photo-generated highly reactive species (•OH and O₂^{-•}) react with RhB dye and degrade it into smaller molecules, eventually forming CO₂ and H₂O (steps 4 and 5).



The surface modification of TiO₂ through AA bridging enhanced the adhesive strength of SnP photosensitizers and optimized its surface properties. During the photocatalytic process, it is possible that the bridging–anchoring groups strongly inhibited the detachment of SnP from the surface of modified TiO₂. And the robustly strong adhesion between SnP and AA@TiO₂ not only increases the amount of SnP attached to the surface of AA@TiO₂ but also accelerates electron transfer from excited SnP to the conduction band of TiO₂.

To detect the photo-generated reactive species during the photocatalytic degradation of RhB dye, we used radical trapping experiments [68,69]. For this purpose, *tert*-butanol (^tBuOH) was used to capture hydroxyl radicals (•OH); *para*-benzoquinone (*p*-BQ) was used for superoxide radical anions (O₂^{-•}); NaN₃ for singlet oxygen; and ethylenediaminetetraacetic acid disodium (Na₂-EDTA) was used to capture photogenerated holes (h⁺) during the photodegradation of RhB dye in the presence of SnP/AA@TiO₂. Figure S14 reveals that the RhB dye degradation rate was critically affected in the presence of ^tBuOH, Na₂-EDTA and *p*-BQ. The degradation of RhB dye was not affected by the presence of NaN₃ or singlet oxygen. Photogenerated holes (h⁺) are the major reactive species compared to hydroxyl radicals (•OH) or superoxide radicals (O₂^{-•}), which are responsible for the catalytic degradation of RhB dye in aqueous solution. The photocatalytic activity of SnP/AA@TiO₂ in RhB degradation under irradiation with monochromatic light at different wavelengths was also investigated (Figure S15). The variation in the wavelength-dependent photodegradation of RhB dye demonstrated that optical absorption makes a significant contribution to solar energy conversion and photocatalytic performance. SnP/AA@TiO₂ showed some degradation ability even at λ > 700 nm.

To identify the degradation products of RhB dye after visible-light irradiation in the presence of SnP/AA@TiO₂, the reaction mixture was withdrawn after 40 min for each photo-degradation experiment and analyzed by ESI-mass spectrometry (Figure S16). The new peaks appearing in the mass spectra confirmed the degradation of RhB dye to new, smaller molecules [70]. Based on the mass spectrum in Figure S16, possible intermediates for the degradation of RhB dye are shown in Figure 6. The initially observed base peak (*m/z* = 443.2; a cationic form of RhB) belongs to the RhB dye. RhB dye can undergo N-

de-ethylation and fragment into smaller parts (m/z 415.2 and m/z 387.2). Finally, all four N-de-ethylation steps lead to the product with m/z 331.1. This cationic species fragmented further after cleavage of the chromophoric group to smaller molecules (m/z 115.0, 166.9, 110.0). These low-molecular-weight aromatic compounds can undergo successive ring cleavage and hydrolysis, thereby forming low-molecular-weight compounds (m/z 119.0, 105.0). Finally, all these intermediate molecules were further disintegrated and mineralized into CO_2 and H_2O . Furthermore, the total organic carbon (TOC) was estimated to calculate the removal of RhB dye by the photocatalysts [71]. The TOC removal percentage obtained with SnP/AA@TiO₂ was only 81%. The TOC removal was 78% for SnP@TiO₂.

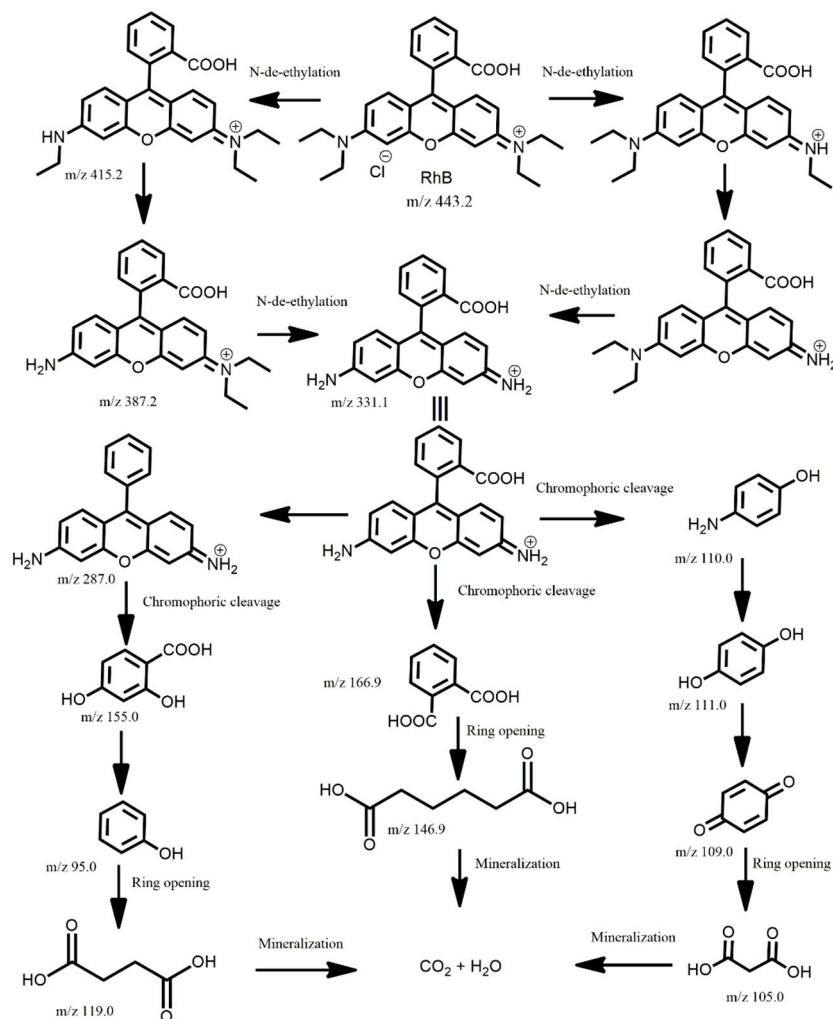


Figure 6. Possible intermediates for the degradation of RhB dye in the presence of composite SnP/AA@TiO₂ photocatalyst.

3. Materials and Methods

TiO₂ (P-25, Degussa, average particle size 100–300 nm) was purchased from commercial suppliers. All purchased chemicals were used without further purification unless otherwise specified. Toluene and pyrrole were distilled from a solution of calcium hydride. (*trans*-Dihydroxo)(5,15,10,20-tetraphenylporphyrinato)tin(IV) (SnP) was synthesized according to our previously reported procedure [36]. Fourier-transform infrared (FT-IR) spectra (KBr) were measured using a Shimadzu FTIR-8400S spectrophotometer (Shimadzu, Tokyo, Japan). Steady-state UV-vis spectra were measured on a Shimadzu UV-3600 spectrophotometer (Shimadzu, Tokyo, Japan). Fluorescence spectra were measured with a Shimadzu RF-5301PC fluorescence spectrophotometer (Shimadzu, Tokyo, Japan). Thermogravimetric analysis (TGA) was recorded using an Auto-TGA Q500 instrument (TA

Instruments, New Castle, DE, USA) at a scan rate of 10 °C/min in the range of 30–600 °C, under an N₂ atmosphere. The Brunauer–Emmett–Teller (BET) surface area was calculated with an analyzer (BELSORP-mini volumetric adsorption equipment) by acquiring N₂ adsorption isotherms at 77 K. The data for the catalyst surface were obtained by using an Autosorb-iQ and Quadrasorb SI apparatus. Powder X-ray diffraction (PXRD) patterns were determined on a Bruker AXS D8 Advance powder X-ray diffractometer (Bruker, Billerica, MA, USA). The morphology and elemental distribution of the synthesized samples were examined using field-emission scanning electron microscopy (FE-SEM) (MAIA III, TESCAN, Brno, Czech Republic) with energy dispersive X-ray spectroscopy (EDS). All samples were deposited on the surface of copper tape by using the drop-casting method. The zeta potential was measured using an Otsuka Electronics ELSZ-2 instrument. Inductively coupled plasma (ICP) analyses were performed on an ICP-Spectrociros CCD instrument.

3.1. Synthesis of SnP/AA@TiO₂

TiO₂ (1.0 g, 12.5 mmol) was added to a solution of adipic acid (1.83 g, 12.5 mmol) dissolved in tetrahydrofuran (THF, 20 mL) and stirred for 6 h at room temperature. The solid materials were filtered and washed with THF and then dried under vacuum for over 2 h at 70 °C. The resulting solid was added to a solution of SnP (0.30 g, 0.39 mmol) dissolved in CH₂Cl₂ (40 mL). The reaction mixture was stirred for 12 h at 25 °C. After that, the solid was filtered, washed with CH₂Cl₂ and dried in a vacuum oven for 6 h at 90 °C. SnP/AA@TiO₂ powder was obtained with a yield of 1.101 g.

3.2. Synthesis of SnP@TiO₂

TiO₂ (1.0 g, 12.5 mmol) was added to a solution of SnP (0.30 g, 0.39 mmol) dissolved in CH₂Cl₂ (40 mL). After that, the reaction mixture was stirred for 12 h at 25 °C. The solid was filtered, washed with CH₂Cl₂ and dried in a vacuum oven for 4 h at 80 °C. SnP@TiO₂ was obtained in a yield of 1.122 g.

3.3. Photocatalytic Degradation Experiment

The photocatalytic efficiency of the synthesized SnP/AA@TiO₂ or SnP@TiO₂ was investigated in the degradation of RhB dye in aqueous solution. The photodegradation reaction of this dye was carried out under irradiation with a 150 W xenon arc lamp with a UV cut-off filter (ABET Technologies, Old Gate Lane Milford, CT, USA) at room temperature (298 K). In a typical procedure, 50 mg of the photocatalyst was added to a 100 mL aqueous solution of RhB (40 mg L⁻¹, distilled water at pH 7) with stirring at room temperature. The reaction mixture remained in the dark for 25 min to reach adsorption–desorption equilibrium. After irradiation with visible light, 3 mL of the suspension was collected at regular intervals. The photocatalyst was collected from the solution by centrifugation followed by filtration using filter paper. The concentration of RhB was examined by determining the absorbance at 554 nm using a UV-vis spectrophotometer.

4. Conclusions

A visible-light-active photocatalyst, SnP/AA@TiO₂, was fabricated by utilizing the coordination chemistry between the axial hydroxo-ligand in the (*trans*-dihydroxo)(5,10,15,20-tetraphenylporphyrinato)Sn(IV) complex (SnP) and adipic acid (AA) on the surface of TiO₂ nanoparticles. The SnP center was tightly coupled to the TiO₂ nanoparticles via an adipic acid linkage in SnP/AA@TiO₂, as judged by various instrumental techniques. Compared to SnP, TiO₂ and SnP@TiO₂, SnP/AA@TiO₂ exhibited remarkably enhanced photocatalytic efficiency for the degradation of rhodamine B dye (RhB) under visible-light irradiation in aqueous solution. The high dye degradation efficiency, low catalyst loading and high reusability make this photocatalyst more efficient than other conventional photocatalysts, such as TiO₂ and ZnO. This work provides a new route for the design of high-efficiency porphyrin-based photocatalytic systems and holds great importance for extending applica-

tions in the field of environmental remediation. The catalyst can prospectively be used as an alternative to so-called conventional photocatalysts.

Supplementary Materials: The following supporting information can be downloaded at: <https://www.mdpi.com/article/10.3390/inorganics11080336/s1>, Figure S1. Energy dispersive X-ray spectroscopy (EDS) elemental maps (C, N, O, Ti, and Sn) of SnP/AA@TiO₂. Figure S2. TGA curves of TiO₂, SnP@TiO₂, and SnP/AA@TiO₂. Figure S3. N₂ adsorption-desorption isotherms of SnP@TiO₂ and SnP/AA@TiO₂. Figure S4. RhB adsorption ability of SnP, TiO₂, SnP@TiO₂, and SnP/AA@TiO₂. Figure S5. Photocatalytic degradation of RhB dye in aqueous solution by SnP/AA@TiO₂ under visible-light irradiation. Figure S6. Kinetics for the photocatalytic degradation of RhB dye by SnP, TiO₂, SnP@TiO₂, and SnP/AA@TiO₂ photocatalysts under visible-light irradiation. Figure S7. Comparison of RhB dye degradation in presence of SnP, TiO₂, and SnP/AA@TiO₂ with various wt% of SnP with respect to TiO₂. Figure S8. Recyclability of SnP/AA@TiO₂ composite photocatalyst in RhB degradation. Figure S9. XRD of SnP/AA@TiO₂ composite photocatalyst before and after RhB degradation. Figure S10. FE-SEM images of SnP/AA@TiO₂ composite photocatalyst before and after RhB degradation. Figure S11. Effect of temperature on RhB degradation in the presence of SnP/AA@TiO₂ composite photocatalyst. Figure S12. Effect of pH of the solution on RhB degradation in the presence of SnP/AA@TiO₂ composite photocatalyst. Figure S13. Effect of initial concentration of RhB on dye degradation using 50 mg of SnP/AA@TiO₂ composite photocatalyst. Figure S14. Photocatalytic degradation of RhB dye in aqueous solution by SnP/AA@TiO₂ composite photocatalyst with the addition of different scavengers under visible-light irradiation ([Na₂-EDTA]₀ = [p-BQ]₀ = [t-BuOH]₀ = 5 mM, pH 7.0, T = 298 K). Figure S15. Photocatalytic activity of SnP/AA@TiO₂ at different wavelengths for the degradation of RhB dye. Figure S16. ESI-MS spectrum (positive ion mode) of the reaction mixture of RhB dye with the SnP/AA@TiO₂ composite photocatalyst after 40 min of visible-light irradiation.

Author Contributions: Investigation, Data curation, Methodology, Software, Validation, Analysis, Writing—original draft, N.K.S.; Project administration, Conceptualization, Supervision, Validation, Funding acquisition, and Writing, editing, and review, H.-J.K. All authors have read and agreed to the published version of the manuscript.

Funding: This work was supported by the National Research Foundation of Korea (NRF) (grant no. 2022R1F1A1074420) funded by the Korean government (MSIT).

Data Availability Statement: Not applicable.

Conflicts of Interest: The authors declare no conflict of interest.

References

1. Wang, Z.; Walker, G.W.; Muir, D.C.G.; Nagatani-Yoshida, K. Toward a Global Understanding of Chemical Pollution: A First Comprehensive Analysis of National and Regional Chemical Inventories. *Environ. Sci. Technol.* **2020**, *54*, 2575–2584. [[CrossRef](#)]
2. Naidu, R.; Biswas, B.; Willett, I.R.; Cribb, J.; Kumar Singh, B.; Paul Nathanail, C.; Coulon, F.; Semple, K.T.; Jones, K.C.; Barclay, A.; et al. Chemical pollution: A growing peril and potential catastrophic risk to humanity. *Environ. Int.* **2021**, *156*, 106616. [[CrossRef](#)]
3. Ren, G.; Han, H.; Wang, Y.; Liu, S.; Zhao, J.; Meng, X.; Li, Z. Recent Advances of Photocatalytic Application in Water Treatment: A Review. *Nanomaterials* **2021**, *11*, 1804.
4. Parvulescu, V.I.; Epron, F.; Garcia, H.; Granger, P. Recent Progress and Prospects in Catalytic Water Treatment. *Chem. Rev.* **2022**, *122*, 2981–3121. [[CrossRef](#)]
5. Rao, C.; Zhou, L.; Pan, Y.; Lu, C.; Qin, X.; Sakiyama, H.; Muddassir, M.; Liu, J. The Extra-Large Calixarene-Based MOFs-Derived Hierarchical Composites for Photocatalysis of Dye: Facile Syntheses and Contribution of Carbon Species. *J. Alloys Compd.* **2022**, *897*, 163178. [[CrossRef](#)]
6. Hollender, J.; Zimmermann, S.G.; Koepke, S.; Krauss, M.; McArdeell, C.S.; Ort, C.; Singer, H.; von Gunten, U.; Siegrist, H. Elimination of Organic Micropollutants in a Municipal Wastewater Treatment Plant Upgraded with a Full-Scale Post-Ozonation Followed by Sand Filtration. *Environ. Sci. Technol.* **2009**, *43*, 7862–7869.
7. Xu, Q.; Huang, Q.-S.; Luo, T.-Y.; Wu, R.-L.; Wei, W.; Ni, B.-J. Coagulation removal and photocatalytic degradation of microplastics in urban waters. *Chem. Eng. J.* **2021**, *416*, 129123.
8. Dong, X.; Li, Y.; Li, D.; Liao, D.; Qin, T.; Prakash, O.; Kumar, A.; Liu, J. A new 3D 8-connected Cd(II) MOF as a potent photocatalyst for oxytetracycline antibiotic degradation. *CrystEngComm* **2022**, *24*, 6933. [[CrossRef](#)]
9. Saratale, R.G.; Saratale, G.D.; Chang, J.S.; Govindwar, S.P. Bacterial decolorization and degradation of azo dyes: A review. *J. Taiwan Inst. Chem. Eng.* **2011**, *42*, 138–157. [[CrossRef](#)]

10. Łuba, M.; Mikołajczyk, T.; Pierożyński, B.; Smoczyński, L.; Wojtacha, P.; Kuczyński, M. Electrochemical Degradation of Industrial Dyes in Wastewater through the Dissolution of Aluminum Sacrificial Anode of Cu/Al Macro-Corrosion Galvanic Cell. *Molecules* **2020**, *25*, 4108.
11. Deng, Y.; Zhao, R. Advanced Oxidation Processes (AOPs) in Wastewater Treatment. *Curr. Pollut. Rep.* **2015**, *1*, 167–176. [[CrossRef](#)]
12. Cardoso, I.M.F.; Cardoso, R.M.F.; da Silva, J.C.G.E. Advanced Oxidation Processes Coupled with Nanomaterials for Water Treatment. *Nanomaterials* **2021**, *11*, 2045. [[CrossRef](#)]
13. Palma, D.; Deganello, F.; Liotta, L.F.; La Parola, V.; Bianco Prevot, A.; Malandrino, M.; Laurenti, E.; Boffa, V.; Magnacca, G. Main Issues in the Synthesis and Testing of Thermocatalytic Ce-Doped SrFeO₃ Perovskites for Wastewater Pollutant Removal. *Inorganics* **2023**, *11*, 85. [[CrossRef](#)]
14. Franco, P.; Sacco, O.; De Marco, I.; Vaiano, V. Zinc Oxide Nanoparticles Obtained by Supercritical Anti solvent Precipitation for the Photocatalytic Degradation of Crystal Violet Dye. *Catalysts* **2019**, *9*, 346. [[CrossRef](#)]
15. Bakbolat, B.; Daulbayev, C.; Sultanov, F.; Beissenov, R.; Umirzakov, A.; Mereke, A.; Bekbaev, A.; Chuprakov, I. Recent Developments of TiO₂-Based Photocatalysis in the Hydrogen Evolution and Photodegradation: A Review. *Nanomaterials* **2020**, *10*, 1790. [[CrossRef](#)]
16. Ong, W.J.; Tan, L.L.; Ng, Y.H.; Yong, S.T.; Chai, S.P. Graphitic Carbon Nitride (g-C₃N₄)-Based Photocatalysts for Artificial Photosynthesis and Environmental Remediation: Are We a Step Closer to Achieving Sustainability. *Chem. Rev.* **2016**, *116*, 7159–7329. [[CrossRef](#)]
17. Guang, H.; Yang, J.; Duan, X.; Farnood, R.; Yang, C.; Yang, J.; Liu, W.; Liu, Q. Recent developments and challenges in zeolite-based composite photocatalysts for environmental applications. *Chem. Eng. J.* **2021**, *417*, 129209.
18. Jin, J.C.; Wang, J.; Guo, J.; Yan, M.H.; Wang, J.; Srivastava, D.; Kumar, A.; Sakiyama, H.; Muddassir, M.; Pan, Y. A 3D rare cubane-like tetramer Cu(II)-based MOF with 4-fold dia topology as an efficient photocatalyst for dye degradation. *Colloids Surf. A* **2023**, *656*, 130475. [[CrossRef](#)]
19. Subhiksha, V.; Kokilavani, S.; Khan, S.S. Recent advances in degradation of organic pollutant in aqueous solutions using bismuth based photocatalysts: A review. *Chemosphere* **2022**, *290*, 133228. [[CrossRef](#)]
20. Heng, Z.W.; Chong, W.C.; Pang, Y.L.; Koo, C.H. An Overview of the Recent Advances of Carbon Quantum Dots/metal Oxides in the Application of Heterogeneous Photocatalysis in Photodegradation of Pollutants towards Visible-Light and Solar Energy Exploitation. *J. Environ. Chem. Eng.* **2021**, *9*, 105199. [[CrossRef](#)]
21. Yao, S.; Yuan, X.; Jiang, L.; Xiong, T.; Zhang, J. Recent Progress on Fullerene-Based Materials: Synthesis, Properties, Modifications, and Photocatalytic Applications. *Materials* **2020**, *13*, 2924. [[CrossRef](#)]
22. Sandhu, I.S.; Chitkara, M.; Rana, S.; Dhillon, G.; Taneja, A.; Kumar, S. Photocatalytic performances of stand-alone graphene oxide (GO) and reduced graphene oxide (rGO) nanostructures. *Opt Quant Electron* **2020**, *52*, 359. [[CrossRef](#)]
23. La, D.D.; Ngo, H.H.; Nguyen, D.D.; Tran, N.T.; Vo, H.T.; Nguyen, X.H.; Chang, S.W.; Chung, W.J.; Nguyen, M.D. Advances and prospects of porphyrin-based nanomaterials via self-assembly for photocatalytic applications in environmental treatment. *Coord. Chem. Rev.* **2022**, *463*, 214543.
24. Schneider, J.; Matsuoka, M.; Takeuchi, M.; Zhang, J.; Horiuchi, Y.; Anpo, M.; Bahnemann, D.W. Understanding TiO₂ Photocatalysis: Mechanisms and Materials. *Chem. Rev.* **2014**, *114*, 9919–9986. [[CrossRef](#)]
25. Drain, C.M.; Varotto, A.; Radivojevic, I. Self-Organized Porphyrinic Materials. *Chem. Rev.* **2009**, *109*, 1630–1658. [[CrossRef](#)]
26. Hasobe, T. Porphyrin-Based Supramolecular Nanoarchitectures for Solar Energy Conversion. *J. Phys. Chem. Lett.* **2013**, *4*, 1771–1780. [[CrossRef](#)]
27. Drain, C.M.; Lehn, J.M. Self-assembly of Square Multiporphyrin Arrays by Metal Ion Coordination. *J. Chem. Soc. Chem. Commun.* **1994**, *19*, 2313–2315. [[CrossRef](#)]
28. Hiroto, S.; Miyake, Y.; Shinokubo, H. Synthesis and functionalization of porphyrins through organometallic methodologies. *Chem. Rev.* **2017**, *117*, 2910–3043. [[CrossRef](#)]
29. Mota, H.P.; Quadrado, R.F.N.; Iglesias, B.A.; Fajardo, A.R. Enhanced photocatalytic degradation of organic pollutants mediated by Zn(II)-porphyrin/poly(acrylic acid) hybrid microparticles. *Appl. Catal. B Environ.* **2020**, *277*, 119208. [[CrossRef](#)]
30. Liu, S.; Xia, S.; Wang, J.; Ren, X.; Chen, S.; Zhong, Y.; Bai, F. Synthesis of the ZnTPyP/WO₃ nanorod-on-nanorod heterojunction direct Z-scheme with spatial charge separation ability for enhanced photocatalytic hydrogen generation. *Nanoscale* **2023**, *15*, 2871–2881. [[CrossRef](#)]
31. Nadeem, S.; Mutalib, I.A.; Shahrin, M.S. Synthesis of Metalloporphyrin Encapsulated Zeolite A for Photocatalytic Orange II Degradation. *Procedia Eng.* **2016**, *148*, 1282–1288. [[CrossRef](#)]
32. Min, K.S.; Kumar, R.S.; Lee, J.H.; Kim, K.S.; Lee, S.G.; Son, Y.A. Synthesis of new TiO₂/porphyrin-based composites and photocatalytic studies on methylene blue degradation. *Dyes Pigments* **2019**, *160*, 37–47. [[CrossRef](#)]
33. La, D.D.; Hangarge, R.V.; Bhosale, S.V.; Ninh, H.D.; Jones, L.A.; Bhosale, S.V. Arginine-Mediated Self-Assembly of Porphyrin on Graphene: A Photocatalyst for Degradation of Dyes. *Appl. Sci.* **2017**, *7*, 643. [[CrossRef](#)]
34. Zhang, J.; Wang, A.; Zhao, W.; Li, C.; Chen, X.; Wang, Y.; Zhu, W.; Zhong, Q. Influence of Metal-Porphyrins on the Photocatalysis of Graphitic Carbon Nitride. *Dyes Pigment.* **2018**, *153*, 241–247. [[CrossRef](#)]
35. Vo, H.T.; Nguyen, A.T.; Tran, C.V.; Nguyen, S.X.; Tung, N.T.; Pham, D.T.; Nguyen, D.D.; La, D.D. Self-Assembly of Porphyrin Nanofibers on ZnO Nanoparticles for the Enhanced Photocatalytic Performance for Organic Dye Degradation. *ACS Omega* **2021**, *6*, 23203–23210. [[CrossRef](#)]

36. Kim, W.; Tachikawa, T.; Majima, T.; Li, C.; Kim, H.-J.; Choi, W. Tin-porphyrin sensitized TiO₂ for the production of H₂ under visible light. *Energy Environ. Sci.* **2010**, *3*, 1789–1795. [[CrossRef](#)]
37. Duan, M.Y.; Li, J.; Mele, G.; Wang, C.; Lu, X.F.; Vasapollo, G.; Zhang, F.X. Photocatalytic Activity of Novel Tin Porphyrin/TiO₂ Based Composites. *J. Phys. Chem. C* **2010**, *114*, 7857–7862. [[CrossRef](#)]
38. Kumar, R.S.; Kim, H.; Mergu, N.; Son, Y.-A. A photocatalytic comparison study between tin complex and carboxylic acid derivatives of porphyrin/TiO₂ composites. *Res. Chem. Intermed.* **2020**, *46*, 313–328. [[CrossRef](#)]
39. Zhang, J.; Zhang, L.; Li, X.; Kang, S.-Z.; Mu, J. Visible Light Photocatalytic Activity of Porphyrin Tin(IV) Sensitized TiO₂ Nanoparticles for the Degradation of 4-Nitrophenol and Methyl Orange. *J. Dispersion Sci. Technol.* **2011**, *32*, 943–947. [[CrossRef](#)]
40. Shee, N.K.; Kim, M.K.; Kim, H.-J. Supramolecular Porphyrin Nanostructures Based on Coordination-Driven Self-Assembly and Their Visible Light Catalytic Degradation of Methylene Blue Dye. *Nanomaterials* **2020**, *10*, 2314. [[CrossRef](#)] [[PubMed](#)]
41. Shee, N.K.; Kim, H.-J. Self-Assembled Nanomaterials Based on Complementary Sn(IV) and Zn(II)-Porphyrins, and Their Photocatalytic Degradation for Rhodamine B Dye. *Molecules* **2021**, *26*, 3598. [[CrossRef](#)] [[PubMed](#)]
42. Shee, N.K.; Kim, H.-J. Sn(IV)-Porphyrin-Based Nanostructures Featuring Pd(II)-Mediated Supramolecular Arrays and Their Photocatalytic Degradation of Acid Orange 7 Dye. *Int. J. Mol. Sci.* **2022**, *23*, 13702. [[CrossRef](#)]
43. Shee, N.K.; Kim, H.-J. Supramolecular squares of Sn(IV)porphyrins with Re(I)-corners for the fabrication of self-assembled nanostructures performing photocatalytic degradation of Eriochrome Black T dye. *Inorg. Chem. Front.* **2023**, *10*, 174–183. [[CrossRef](#)]
44. Shee, N.K.; Park, B.-H.; Kim, H.-J. Hybrid Composite of Sn(IV)-Porphyrin and Mesoporous Structure for Enhanced Visible Light Photocatalytic Degradation of Organic Dyes. *Molecules* **2023**, *28*, 1886. [[CrossRef](#)]
45. Fallon, G.D.; Langford, S.J.; Lee, M.A.-P.; Lygris, E. Self-assembling Mixed Porphyrin Trimers—The Use of Diaxial Sn(IV) Porphyrin Phenolates as an Organising Precept. *Inorg. Chem. Commun.* **2002**, *5*, 715–718. [[CrossRef](#)]
46. Hawley, J.C.; Bampos, N.; Sanders, J.K.M. Synthesis and Characterization of Carboxylate Complexes of Sn^{IV} Porphyrin Monomers and Oligomers. *Chem. Eur. J.* **2003**, *9*, 5211–5222.
47. Arnold, D.P.; Blok, J. The coordination chemistry of tin porphyrin complexes. *Coord. Chem. Rev.* **2004**, *248*, 299–319. [[CrossRef](#)]
48. Ou, Z.; E, W.; Zhu, W.; Thordarson, P.; Sintic, P.J.; Crossley, M.J.; Kadish, K.M. Effect of Axial Ligands and Macrocyclic Structure on Redox Potentials and Electron-Transfer Mechanisms of Sn(IV) Porphyrins. *Inorg. Chem.* **2007**, *46*, 10840–10849. [[CrossRef](#)]
49. Shetti, V.S.; Ravikanth, M. Sn(IV) Porphyrin based axial-bonding type porphyrin triads containing heteroporphyrins as axial ligands. *Inorg. Chem.* **2010**, *49*, 2692–2700. [[CrossRef](#)]
50. Sharma, R.; Ghosh, A.; Wolfram, B.; Bröring, M.; Ravikanth, M. Synthesis and Characterization of Hexa-Coordinated Sn(IV) Complexes of Meso-Aryl Dipyrins. *Dalton Trans.* **2013**, *42*, 5627–5630. [[CrossRef](#)]
51. Pareek, Y.; Lakshmi, V.; Ravikanth, M. Axially bonded pentads constructed on the Sn(IV) porphyrin scaffold. *Dalton Trans.* **2014**, *43*, 6870–6879. [[CrossRef](#)]
52. Natali, M.; Amati, A.; Demitri, N.; Iengo, E. Formation of a Long-Lived Radical Pair State in a Sn(IV) Porphyrin-di-(L-tyrosinato) Conjugate Driven by Proton-Coupled Electron-Transfer. *Chem. Commun.* **2018**, *54*, 6148–6152. [[CrossRef](#)]
53. Ravikumar, M.; Raghav, D.; Rathinasamy, K.; Kathiravan, A.; Mothi, E.M. DNA Targeting Long-Chain Alkoxy Appended Tin(IV) Porphyrin Scaffolds: Photophysical and Antimicrobial PDT Investigations. *ACS Appl. Bio Mater.* **2018**, *1*, 1705–1716. [[CrossRef](#)] [[PubMed](#)]
54. Shee, N.K.; Kim, M.K.; Kim, H.-J. Fluorescent chemosensing for aromatic compounds by supramolecular complex composed of tin(IV) porphyrin, viologen, and cucurbit[8]uril. *Chem. Commun.* **2019**, *55*, 10575–10578. [[CrossRef](#)]
55. Chatterjee, S.; Tyagi, A.K.; Ayyub, P. Efficient Photocatalytic Degradation of Rhodamine B Dye by Aligned Arrays of Self Assembled Hydrogen Titanate Nanotubes. *J. Nanomater.* **2014**, *2014*, 328618. [[CrossRef](#)]
56. Sundararajan, M.; Sailaja, V.; Kennedy, L.J.; Vijaya, J.J. Photocatalytic degradation of Rhodamine B under visible light using nanostructured zinc doped cobalt ferrite: Kinetics and mechanism. *Ceram. Int.* **2017**, *43*, 540–548. [[CrossRef](#)]
57. Zhao, G.; Zou, J.; Li, C.; Yu, J.; Jiang, X.; Zheng, Y.; Hu, W.; Jiao, F. Enhanced photocatalytic degradation of rhodamine B, methylene blue and 4-nitrophenol under visible light irradiation using TiO₂/MgZnAl layered double hydroxide. *J. Mater. Sci. Mater. Electron.* **2018**, *29*, 7002–7014. [[CrossRef](#)]
58. Luna-Flores, A.; Morales, M.A.; Agustín-Serrano, R.; Portillo, R.; Luna-López, J.A.; Pérez-Sánchez, G.F.; Luz, A.D.H.-d.l.; Tepale, N. Improvement of the Photocatalytic Activity of ZnO/Burkeite Heterostructure Prepared by Combustion Method. *Catalysts* **2019**, *9*, 817. [[CrossRef](#)]
59. Pontes do Nascimento, N.M.; Machado de Lima, B.R.; Zamian, J.R.; Ferreira da Costa, C.E.; Adriano Santos do Nascimento, L.; Luque, R.; Filho, G.N.d.R. Synthesis of Mesoporous Zn_{1-x}M_xAl₂O₄ Substituted by Co²⁺ and Ni²⁺ Ions and Application in the Photodegradation of Rhodamine B. *Materials* **2020**, *13*, 2150. [[CrossRef](#)]
60. Huang, J.; Nie, G.; Ding, Y. Metal-Free Enhanced Photocatalytic Activation of Dioxygen by g-C₃N₄ Doped with Abundant Oxygen-Containing Functional Groups for Selective N-Deethylation of Rhodamine B. *Catalysts* **2020**, *10*, 6. [[CrossRef](#)]
61. Suvaitha, P.; Selvam, S.; Ganesan, D.; Rajangam, V.; Raji, A. Green Synthesis of SnO₂ Nanoparticles for Catalytic Degradation of Rhodamine B. *Iran. J. Sci. Technol. Trans. A Sci.* **2020**, *44*, 661–676.
62. Zhou, C.; Liu, Z.; Fang, L.; Guo, Y.; Feng, Y.; Yang, M. Kinetic and Mechanistic Study of Rhodamine B Degradation by H₂O₂ and Cu/Al₂O₃/g-C₃N₄ Composite. *Catalysts* **2020**, *10*, 317. [[CrossRef](#)]

63. Ahmad, M.; Rehman, W.; Khan, M.M.; Qureshi, M.T.; Gul, A.; Haq, S.; Ullah, R.; Rab, A.; Mena, F. Phytogetic fabrication of ZnO and gold decorated ZnO nanoparticles for photocatalytic degradation of Rhodamine B. *J. Environ. Chem. Eng.* **2021**, *9*, 104725. [[CrossRef](#)]
64. Alorku, K.; Manoj, M.; Yanjuan, C.; Zhou, H.; Yuan, A. Nanomixture of 0-D ternary metal oxides (TiO₂-SnO₂-Al₂O₃) cooperating with 1-D hydroxyapatite (HAp) nanorods for RhB removal from synthetic wastewater and hydrogen evolution via water splitting. *Chemosphere* **2021**, *273*, 128575. [[CrossRef](#)]
65. Amakali, T.; Živković, A.; Warwick, M.E.A.; Jones, D.R.; Dunnill, C.W.; Daniel, L.S.; Uahengo, V.; Mitchell, C.E.; Dzade, N.Y.; de Leeuw, N.H. Photocatalytic degradation of rhodamine B dye and hydrogen evolution by hydrothermally synthesized NaBH₄-spiked ZnS nanostructures. *Front. Chem.* **2022**, *10*, 835832. [[CrossRef](#)]
66. Rojas-García, E.; García-Martínez, D.C.; López-Medina, R.; Rubio-Marcos, F.; Castañeda-Ramírez, A.A.; Maubert-Franco, A.M. Photocatalytic Degradation of Dyes Using Titania Nanoparticles Supported in Metal-Organic Materials Based on Iron. *Molecules* **2022**, *27*, 7078. [[CrossRef](#)] [[PubMed](#)]
67. Liu, D.; Song, J.; Chung, J.S.; Hur, S.H.; Choi, W.M. ZnO/Boron Nitride Quantum Dots Nanocomposites for the Enhanced Photocatalytic Degradation of Methylene Blue and Methyl Orange. *Molecules* **2022**, *27*, 6833. [[CrossRef](#)] [[PubMed](#)]
68. Benhebal, H.; Wolfs, C.; Kadi, S.; Tilkin, R.G.; Allouche, B.; Belabid, R.; Collard, V.; Felten, A.; Louette, P.; Lambert, S.D.; et al. Visible Light Sensitive SnO₂/ZnCo₂O₄ Material for the Photocatalytic Removal of Organic Pollutants in Water. *Inorganics* **2019**, *7*, 77. [[CrossRef](#)]
69. Xu, J.; Gao, Q.; Wang, Z.; Zhu, Y. An all-organic 0D/2D supramolecular porphyrin/g-C₃N₄ heterojunction assembled via π - π interaction for efficient visible photocatalytic oxidation. *Appl. Catal. B* **2021**, *291*, 120059. [[CrossRef](#)]
70. Yang, J.; Zhu, H.; Peng, Y.; Li, P.; Chen, S.; Yang, B.; Zhang, J. Photocatalytic Performance and Degradation Pathway of Rhodamine B with TS-1/C₃N₄ Composite under Visible Light. *Nanomaterials* **2020**, *10*, 756. [[CrossRef](#)]
71. Alharthi, F.A.; Ababtain, A.S.; Aldubeikl, H.K.; Alanazi, H.S.; Hasan, I. Deep Eutectic Solvent-Mediated Synthesis of Ni₃V₂O₈/N-Doped RGO for Visible-Light-Driven H₂ Evolution and Simultaneous Degradation of Dyes. *Inorganics* **2023**, *11*, 67. [[CrossRef](#)]

Disclaimer/Publisher's Note: The statements, opinions and data contained in all publications are solely those of the individual author(s) and contributor(s) and not of MDPI and/or the editor(s). MDPI and/or the editor(s) disclaim responsibility for any injury to people or property resulting from any ideas, methods, instructions or products referred to in the content.